Simulation of conjugate radiation-forced convection heat transfer in a porous medium using the lattice Boltzmann method

Yousef Kazemian[a], Saman Rashidi[a], Javad Abolfazli Esfahani[a*], and Nader Karimi[b]

[a] Department of Mechanical Engineering, Ferdowsi University of Mashhad, Mashhad 91775-1111, Iran

[b] School of Engineering, University of Glasgow, Glasgow G12 8QQ, UK

*corresponding author e-mail: abolfazl@um.ac.ir

Abstract

In this paper, a lattice Boltzmann method is employed to simulate the conjugate radiation-forced convection heat transfer in a porous medium. The absorbing, emitting, and scattering phenomena are fully included in the model. The effects of different parameters of a silicon carbide porous medium including porosity, pore size, conduction-radiation ratio, extinction coefficient and kinematic viscosity ratio on the temperature and velocity distributions are investigated. This shows that there is a good agreement between the results obtained by the current LBM and the existing analytical solutions. The convergence times of modified and regular LBMs for this problem are 15s and 94s, respectively, indicating a considerable reduction in the solution time through using the modified LBM. Further, the thermal plume formed behind the porous cylinder elongates as the porosity and pore size increase. This result reveals that the thermal penetration of the porous cylinder increases with increasing the porosity and pore size. Finally, the mean temperature at the channel output increases by about 22% as the extinction coefficient of fluid increases in the range of 0 to 0.03.

Keywords: Lattice Boltzmann; Conjugate radiation-forced convection; Porous medium; Porosity, Conduction radiation ratio

Nomenclature

c_L	Speed of Light
c	Lattice streaming speed
c_0	Parameter defined
c_1	Parameter defined
c_s	Speed of sound
c_k	Lattice speed discreted in the main directions of the Lattice
c_p	Specific heat capacity
Da	Darcy number, $= K/H^2$
Data	Amount of each data per each mesh size
d_p	Pore size diameter
e_i	Discrete particle velocity in LBE model
e_a^{21}	Approximate relative error
e_{ext}^{21}	Extrapolated relative error
F	Total body force vector
f_k	Density distribution function in LBE model
f_k^{eq}	Equilibrium density distribution function in LBE model
F_k	Discrete body force in LBE model
F_ε	Geometric function
g_k	Temperature distribution function in LBE model
g_k^{eq}	Equilibrium temperature distribution function in LBE model
G	Incident radiation
GCI_{fine}^{21}	Fine-grid convergence index
H	Channel height
i	Direction index in LBE model (D2Q8 model)

I	Unit matrix
I_b	Radiation intensity of the black body
I_i	Radiation distribution function in LBE model
I_i^{eq}	Equilibrium radiation distribution function in LBE model
j	Kinematic viscosity ratio
k	Direction index in LBE model (D2Q9 model)
K_a	Absorbing coefficient
L	Channel Length
M	Number of node
$\dot{m}_{in}$	Mass flow rate at the inlet of the channel
$\dot{m}_{sectio}$	Mass flow rate at each section of the channel
N	Conduction radiation ratio $= \frac{k_e \beta_e}{4\sigma(T_w - T_{in})^3}$
Nu	Nusselt number
p	Pressure
P	Apparent order
P_f	Scattering phase function
Pr	Prandtl number,$= \frac{\upsilon_e}{\alpha_e}$
q^r	Dimensionless radiative heat flux
r	Ratio of the number of nodes
$\vec{r}_n$	Position vector
RP	Radiation parameter$= \frac{\beta_f^2(1-\omega)H^2}{4N}$
Re	Reynolds number $= \frac{U_{in}H}{\upsilon_f}$
s	Constant parameter

$\vec{s}$	Geometric distance
t	Time
T	Temperature
T_{in}	Inlet temperature
T_w	Wall temperature
u	Fluid velocity vector
u	Fluid velocity in x direction
u_o	Velocity at outlet
U	Non-dimensional fluid velocity, $= u/U_{in}$
U_{in}	Inlet fluid velocity
$u_{section}$	Local velocity in each section
URF	Under relaxation factor
Δu^+	Velocity difference with inlet section of the channel
v	Temporal velocity vector defined in Eq. (20)
v	Fluid velocity in y direction
w_{gi}	Weighting coefficient for radiation
w_k	Weighting coefficient for energy and momentum
x	Axial coordinate
X	Non-dimensional axial coordinat, $= x/H$
y	Transversal coordinate
Y	Non-dimensional transversal coordinat, $= y/H$

Greek symbols

α_f	Thermal diffusivity coefficient for fluid
α_s	Thermal diffusivity coefficient for solid
α_e	Effective Thermal diffusivity coefficient

Δt	Time step
Δx	Space step
ε	Porosity
ϵ	Difference of data
β_e	Effective Extinction coefficient
β_s	Extinction coefficient for solid
β_f	Extinction coefficient for fluid
υ_e	Effective kinematical viscosity
τ_{α_e}	Effective relaxation time for temperature distribution
τ_{υ_e}	Effective relaxation time for velocity distribution
υ_f	Kinematical viscosity for fluid
γ	Thermal diffusivity ratio
σ	Stefan–Boltzmann constant
σ_s	Scattering coefficient
ε_e	Emissivity coefficient
ω	Scattering albedo
θ	Dimensionless temperature, $= \frac{T-T_{in}}{T_w-T_{in}}$
θ_m	Non-dimensional mean temperature
θ_w	Non-dimensional temperature on the channel wall
K_a	Absorbing coefficient
ρ_{in}	Density at inlet
ρ_o	Density at outlet
Ω	space angle

$\boldsymbol{\gamma}$	polar angle
δ	horizon angle
φ_{ext}^{21}	extrapolated values

1. Introduction

Over the last two decades, the applications of lattice Boltzmann method (LBM) to the simulations of fluid flow and heat transfer have increased significantly. The reason for the popularity of this method with the research communities is the simplicity of algorithms and boundary conditions, as well as ability to model the problems with complex geometries [1-3]. Porous materials and foams are widely used in different thermal systems such as heat exchangers [4], building energy systems [5] and solar thermal systems [6]. Accordingly, investigating the influences of different parameters of these materials on fluid flow and heat transfer is imperative for these applications. So far, researchers have used lattice Boltzmann method in different problems of porous media such as boiling mechanism [7], deposition of particles [8], oscillating flow and heat transfer [9], thermal non-Newtonian fluid flows [10]. Ma et al. [11] used the lattice Boltzmann method to simulate the gas diffusion in isotropic and anisotropic fractal porous media. They concluded that the differences of effective diffusion coefficients for various diffusion directions augment considerably as the anisotropic strength increases. Yun et al. [12] employed the lattice Boltzmann method for Mesoscopic pore-scale simulating the free convection in porous media. They found that the Reynolds number has a considerable effect on free convection in porous media.

Simulation of combined radiation-force convection heat transfer in porous media is of importance in several engineering applications including oil and gas extraction, nuclear reactor, gas storage, chemical reactions, and thermal energy storage [13]. Researchers have already used different numerical, analytical, and experimental methods to investigate this problem. Thakur et al. [14] performed an experimental work to study the solar air heater enhanced with a packed

bed. They found that the volumetric heat transfer coefficient enhances with decreasing the porosity of the packed bed. Dehghan et al. [15] used Homotopy perturbation technique to simulate the combined radiation-force convection heat transfer in a duct as a heat exchanger, filled with porous material. Their results indicated that the Homotopy perturbation as semi-analytical technique is capable of simulating the radiation heat transfer in porous media. In another investigation, Bovand et al. [16] used computational fluid dynamics (CFD) to simulate the combined radiation-force convection heat transfer in a duct both partially and fully filled with porous material. Their results showed that the heat transfer coefficient reduces by increasing the porous layer thickness for smaller values of Darcy number. Parmananda et al. [17] used CFD to simulate the compound influences of convection and radiation in cubical cavities. These authors studied the effects of partitioning on heat transfer and concluded that partitioning along the front and back surfaces provide larger values of radiation and convective heat transfer coefficients in comparison with the top-bottom partitioning. Hosseini et al. [1] used LBM to model the compound radiation-force convection heat transfer inside a clear duct. Their results showed that the entrance length to develop the temperature field reduces as the radiation parameter increases.

There are a number of studies about the applications of LBM in simulation of single-mode heat transfer in porous media. Gao et al. [18] used a new LBM to simulate conjugate convective heat transfer between a porous medium and other media including fluid, solid, and porous media. In their LBM, the volumetric heat capacity and a new parameter were defined for the equilibrium temperature distribution function to satisfy the temperature and heat flux continuities at the interface between the two media. It further does not need any correction of distribution functions around the interface. Vijaybabu et al. [19] used LBM to model the mixed convection heat transfer around a porous square obstacle. They found that for smaller Darcy numbers, e.g. 10^{-6}, the porous obstacle acts as a solid one exerts a larger resistance against the flow.

The literature review showed that currently there is no study on simulating the conjugate radiation-forced convection heat transfer in a porous medium by using lattice Boltzmann method. As stated earlier, the problem of conjugate radiation-forced convection heat transfer in a porous medium is practically important. Beside this, lattice Boltzmann method is a highly capable tool and generally thermal radiation can be readily simulated through using LBM. Further, in this paper, the lattice Boltzmann method is modified to improve the convergence speed and reduce the solution time in this problem. The procedure of this modification is presented in Appendix A.

2. Problem description

A schematic view of the problem under investigation is shown in Fig. 1. In this study, a two-dimensional channel with height H and length L=10H is considered. A circular porous obstacle with diameter H/2 and constant temperature T_w is placed at the distances L/4 and H/2 from the inlet and lower walls of the channel, respectively. Air flows through the channel with uniform inlet velocity U_{in} and inlet temperature T_{in}.

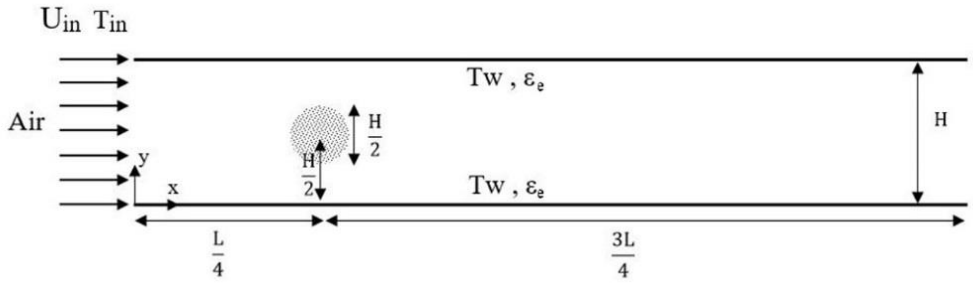

Fig. 1. The schematic view of the problem

3. Mathematical models

3.1. Governing equations

Momentum, energy, and radiation transfer equations are solved by using a Lattice Boltzmann's method (BGK-SRT) [20-21]. The D_2Q_9 model is used to solve the momentum and energy equations. This model is shown in Fig. 2.

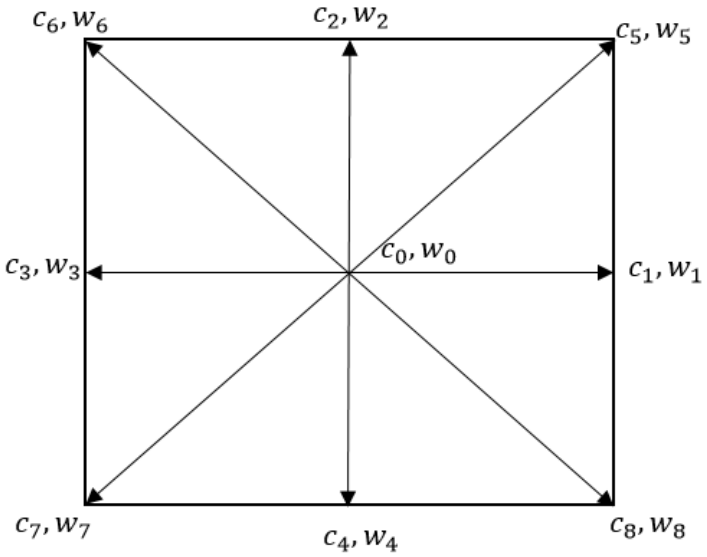

Fig. 2. Schematic of the lattice speed and weighting coefficient for momentum and energy equations.

It should be noted that in this figure, w_k and c_k are the weighting coefficient and lattice speed, respectively. These parameters can be defined as

$$c_k = \begin{cases} 0, & k = 0 \\ \left(\cos\left[\frac{(k-1)\pi}{4}\right], \sin\left[\frac{(k-1)\pi}{4}\right]\right)c, & k = 1, \dots, 4 \\ \sqrt{2}\left(\cos\left[\frac{(k-1)\pi}{4}\right], \sin\left[\frac{(k-1)\pi}{4}\right]\right)c & k = 5, \dots, 8 \end{cases} \quad (1)$$

$$w_k = \begin{cases} \frac{4}{9}, & k = 0 \\ \frac{1}{9}, & k = 1, \dots, 4 \\ \frac{1}{36}, & k = 5, \dots, 8 \end{cases} \quad (2)$$

where c_s denotes the speed of sound (c) and can be related to flow speed by:

$$c_s = \frac{c}{\sqrt{3}}, \qquad c = \frac{\Delta x}{\Delta t}, \quad (3)$$

where Δx and Δt are the lattice space and the time steps, respectively. In this paper, isotropic and equilibrium radiation conditions in an absorbing, emitting, and scattering medium are

assumed. The D_2Q_8 model is used to solve the radiation equation. This model is shown in Fig. 3.

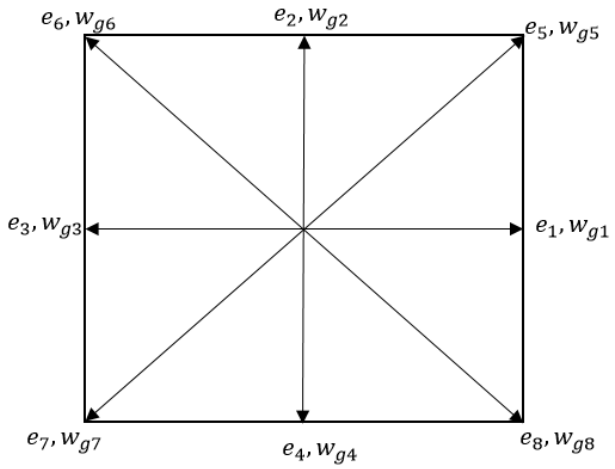

Fig. 3. Schematic of the lattice speed and weighting coefficient for radiation

In this figure, w_{gi} and e_i are the weighting coefficient and velocity along the lattice link i, respectively. These parameters are defined by:

$$w_{gi} = \frac{1}{8}, \tag{4}$$

$$e_{1,3} = (\pm 1, 0) \cdot c\ ,\ e_{2,4} = (0, \pm 1) \cdot c\ ,\ e_{5,6,7,8} = (\pm 1, \pm 1) \cdot c. \tag{5}$$

3.1.1. Momentum equation

The generalised model proposed by Nithiarasu et al. [22] is used to simulate the incompressible fluid flows through stationary porous media. In this approach, the flow is governed by the following Navier-Stokes equation:

$$\frac{\partial \boldsymbol{u}}{\partial t} + (u\,.\nabla)\left(\frac{u}{\varepsilon}\right) = -\frac{1}{\rho}\nabla(\varepsilon p) + \nu_e \nabla^2 u + F, \tag{6}$$

where ρ, u, p, and ν_e are the fluid density, the volume-averaged velocity, pressure, and the effective kinematic viscosity, respectively. Further, F is the total force due to the existence of porous medium and other external forces, which are directly introduced as an external force in Lattice Boltzmann's equations [23-24].

The lattice equation for flow in a porous medium can be solved in two steps including collision and streaming stages. These stages are [25, 26]:

$$f_k(\vec{r}_n + \vec{c}_k \cdot \Delta t, t + \Delta t) - f_k(\vec{r}_n, t) = \frac{1}{\tau_{v_e}}\left(f_k^{eq}(\vec{r}_n, t) - f_k(\vec{r}_n, t)\right) + \Delta t F_k, \quad (7)$$

where F_k is the discrete body force in lattice Boltzmann model and can be defined as follows.

$$F_k = w_k \rho \left(1 - \frac{1}{2\tau_{v_e}}\right)\left[\frac{c_k \cdot F}{c_s^2} + \frac{uF : (c_k c_k - c_s^2 I)}{\varepsilon c_s^4}\right], \quad (8)$$

in which f_k and f_k^{eq} are the distribution function and the equilibrium distribution function, respectively. Further, τ_{v_e} is an effective relaxation time and can be calculated by

$$v_e = \frac{\Delta X^2}{3\Delta t}(\tau_{v_e} - 0.5), \quad (9)$$

where v_e is the effective kinematic viscosity. This parameter can be related to the fluid kinematic viscosity v_f by defining the following kinematic viscosity ratio:

$$j = \frac{v_e}{v_f}. \quad (10)$$

The equilibrium distribution function can be defined by [25]

$$f_k^{eq} = w_k \rho \left[1 + \frac{c_k \cdot u}{c_s^2} + \frac{uu : (c_k c_k - c_s^2 I)}{2\varepsilon c_s^4}\right]. \quad (11)$$

In Eq. 8, F is the total body force induced by the porous medium and other external forces without buoyancy. This parameter can be expressed by [27]:

$$F = -\frac{\varepsilon v_e}{K} u - \frac{\varepsilon F_\varepsilon}{\sqrt{K}} |u| u, \quad (12)$$

where $|u|$ is

$$|u| = \sqrt{u^2 + v^2}. \quad (13)$$

The first and second terms in the right-hand side of Eq. 12 denote Darcy and Forchheimer forces, respectively. Further, K and F_ε are the permeability of the porous medium and geometric function, respectively. According to Ergun's experimental investigations [28], the geometric function and the permeability K are given by [29]:

$$F_\varepsilon = \frac{1.75}{\sqrt{150\varepsilon^3}}, \tag{14}$$

$$K = \frac{\varepsilon^3 d_p^2}{150(1-\varepsilon)^2}. \tag{15}$$

The macroscopic fluid density and pressure are determined by:

$$\rho = \sum_k f_k, \tag{16}$$

$$p = \frac{c_s^2 \rho}{\varepsilon}. \tag{17}$$

The velocity in the porous medium can be determined by using the following nonlinear equation:

$$\rho u = \sum_k c_k f_k + \frac{\Delta t}{2} \rho F, \tag{18}$$

Solving the above equation yields the following relationship:

$$u = \frac{\boldsymbol{v}}{c_0 + \sqrt{c_0^2 + c_1 |\boldsymbol{v}|}}, \tag{19}$$

Note that the procedure for converting Eq. 18 into Eq. 19 is fully presented in Appendix B. Moreover, in Eq. 19, the temporary velocity $\boldsymbol{v}$ and constant parameters c_0 and c_1 are expressed by:

$$\boldsymbol{v} = \frac{\sum_k c_k f_k}{\rho}, \tag{20}$$

$$c_0 = \frac{1}{2}\left(1 + \varepsilon \frac{\Delta t}{2} \frac{v_f}{K}\right), \tag{21}$$

$$c_1 = \varepsilon \frac{\Delta t}{2} \frac{F_\varepsilon}{\sqrt{K}}, \tag{22}$$

in which the temporary velocity, $\boldsymbol{v}$, is a non-corrected velocity vector, which the exact velocity in the porous medium can be determined by placing the temporary velocity in Eq. 19.

The governing equations for the flow inside the porous medium can be used for the flow outside the porous medium by considering ε=1 and F=0. Also, the velocity of the flow outside the porous medium is calculated from Eq. 20.

3.1.2. Energy equation

The energy equation, similar to momentum equation, can be solved in two stages of collision and streaming as follows [30-33]:

$$g_k(\vec{r}_n + \vec{c}_k \cdot \Delta t, t + \Delta t) - g_k(\vec{r}_n, t) = \frac{1}{\tau_{\alpha_e}}\left(g_k^{eq}(\vec{r}_n, t) - g_k(\vec{r}_n, t)\right) - w_k\left(\frac{\Delta t}{\rho c_p}\right)(\nabla \cdot q^r), \quad (23)$$

where g_k and g_k^{eq} are the distribution function and the equilibrium distribution function, respectively. τ_{α_e} is an effective relaxation time which can be defined as

$$\alpha_e = \frac{\Delta X^2}{3\Delta t}\left(\tau_{\alpha_e} - 0.5\right), \quad (24)$$

in which α_e is the effective thermal diffusivity calculated by

$$\alpha_e = \varepsilon\alpha_f + (1-\varepsilon)\alpha_s, \quad (25)$$

where α_s and α_f are the solid and fluid thermal diffusivities, respectively. They can be related to the effective thermal diffusivity by defining the following thermal diffusivity ratio:

$$\gamma = \frac{\alpha_e}{\alpha_f}. \quad (26)$$

In Eq. 24, the equilibrium distribution function can be calculated by [25]:

$$g_k^{eq} = w_k\theta\left[1 + \frac{3}{c^2}c_k \cdot u\right], \quad (27)$$

where in dimensionless temperature of fluid θ is given by

$$\theta = \sum_k g_{k.} \quad (28)$$

In Eq. 23, $\nabla . q^r$ is the radiative source term and is defined as [34]

$$\nabla . q^r = K_a(4\sigma\theta^4 - G), \quad (29)$$

$$K_a = \beta_e(1-\omega), \tag{30}$$

where β_e, K_a ,σ ,G and ω are the effective extinction coefficient, absorption coefficient, Stefan–Boltzmann constant, incident radiation, and scattering albedo, respectively. The relationship between the effective extinction coefficient and the scattering albedo can be found through the following equation:

$$\omega = \frac{\sigma_s}{\beta_e}, \tag{31}$$

where σ_s and G are the scattering coefficient and incident radiation, respectively.

3.1.3. Radiation equations

The transmission equation for the radiation in the desired direction of $\vec{s}$ can be presented in the following form [35]:

$$\frac{dI}{ds} = \vec{s}.\nabla I = -\beta_e I + k_a I_b + \frac{\sigma_s}{4\pi}\int_{4\pi} I P_f\left(\Omega, \acute{\Omega}\right) d\acute{\Omega} \tag{32}$$

where I, β_e, Ω, σ_s, $\vec{s}$, k_a are the radiation intensity, extinction coefficient, space angle, scattering coefficient, the geometric distance in the specified direction, and the absorption coefficient, respectively. Moreover, $I_b = {\sigma T^4}/{\pi}$ and p are the radiation intensity of the black body and the scattering phase function, respectively. For $P_f\left(\Omega, \acute{\Omega}\right) = 1$, the equilibrium radiation conditions are set and as a result, the volume distribution, $4\pi I_b$, is equal to the volume absorption, G, for this problem and the equation can be rewritten in the following form [36]:

$$\frac{dI}{ds} + \vec{s}.\nabla I = \beta_e\left(\frac{G}{4\pi} - I\right) \tag{33}$$

The unsteady equation for I_i, the radiation intensity in the specified direction I, is similarly presented by [36]:

$$\frac{1}{c_L}\frac{\partial I_i}{\partial t} + \vec{s}.\nabla I_i = \beta_e\left(\frac{G}{4\pi} - I_i\right) \tag{34}$$

The radiation equations are similar for the two areas, and only the effective parameters are used for the equations in the porous medium.

Since the geometry is two-dimensional and the lattice Boltzmann method is used, it is necessary to produce a two-dimensional grid that includes the entire plate of the desired domain. Figure 4 shows the employed grid on a plate. In addition, since a two-dimensional radiation heat transfer is considered, all defined radiation directions must be solved. At each point, the radiation takes place in the spherical space of 4π and accordingly, the polar angle, $0 \leq \gamma \leq \pi$, is assumed to be isotropic. Therefore, the angular dependence of the radiation intensity can be assumed to be only in the direction of the angle from the horizon ($0 \leq \delta \leq 2\pi$).

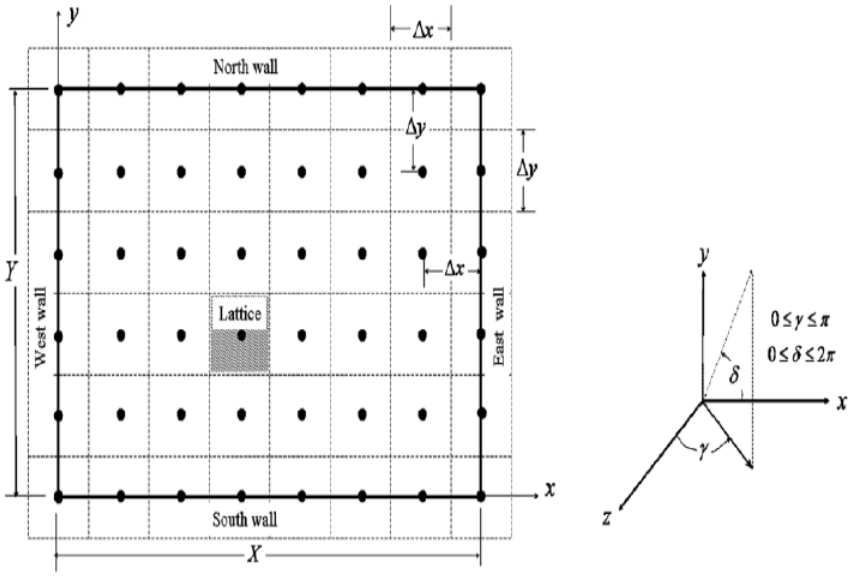

Fig. 4. The grid on a plate to solve the radiation equation.

The details of solving of the radiation equation through LBM are presented in Refs. [37-39]. In lattice Boltzmann method, thermal radiation can be simulated using the following equation.

$$I_i(\vec{r}_n + e_i \cdot \Delta t, t + \Delta t) - I_i(\vec{r}_n, t) = \frac{\Delta t}{\tau_i}\left[I_i^{eq}(\vec{r}_n, t) - I_i(\vec{r}_n, t)\right], \quad (35)$$

where I_i and I_i^{eq} are the distribution function and the equilibrium distribution function, respectively. τ_i is the radiative relaxation time and is given by [37]:

$$\tau_i = \frac{1}{e_i \beta_e}. \tag{36}$$

In Eq. 35, the equilibrium distribution function I^{eq} is determined by:

$$I_i^{eq} = \sum_{i=1}^{8} I_i w_{gi}. \tag{37}$$

In Eq. 29, the source term of energy equation can be calculated by the following expression [40]:

$$I^{eq} = \frac{G}{4\pi}. \tag{38}$$

3.2. Boundary conditions

The boundary conditions for the fluid flow are presented in this section [41]:

- At the inlet section of the channel:

$$\rho_{in} = \frac{f_0 + f_2 + f_4 + 2(f_3 + f_6 + f_7)}{1 - u_{in}} \tag{39}$$

$$f_1 = f_3 + \frac{2}{3}(\rho u)_{in} \tag{40}$$

$$f_5 = f_7 + \frac{1}{6}(\rho u)_{in} \tag{41}$$

$$f_8 = f_6 + \frac{1}{6}(\rho u)_{in} \tag{42}$$

- At the outlet section of the channel:

$$u_o = -1 + \frac{(f_0 + f_2 + f_4 + 2 \times (f_1 + f_5 + f_8))}{\rho_o} \tag{43}$$

$$f_3 = f_1 - \frac{2}{3}\rho_0 u_o \tag{44}$$

$$f_7 = f_5 - \frac{1}{6}\rho_0 u_o + 0.5 \times (f_2 - f_4) \tag{45}$$

$$f_6 = f_8 - \frac{1}{6}\rho_0 u_o + 0.5 \times (f_4 - f_2) \tag{46}$$

- Over the channel walls:

The bounce back boundary conditions are used for the channel walls. This boundary is defined by [41]:

- The bounce back boundary condition for the upper wall:

$$f_4 = f_2 \tag{47}$$

$$f_8 = f_6 + 0.5 \times (f_3 - f_1) \tag{48}$$

$$f_7 = f_5 + 0.5 \times (f_1 - f_3) \tag{49}$$

- The bounce back boundary condition for the lower wall:

$$f_2 = f_4 \tag{50}$$

$$f_6 = f_8 - 0.5 \times (f_3 - f_1) \tag{51}$$

$$f_5 = f_7 - 0.5 \times (f_1 - f_3) \tag{52}$$

Moreover, the following thermal boundary conditions are used [41]:

- At the inlet section of the channel:

$$g_k = \theta_{in}(w_k + w_{\hat{k}}) - g_{\hat{k}} \tag{53}$$

- At the outlet section of the channel:

$$g_{k,n} = 2 \times g_{k,n-1} - g_{k,n-2} \tag{54}$$

where n is the number of nodes in x direction.

- At the channel walls:

$$g_k = \theta_w(w_k + w_{\hat{k}}) - g_{\hat{k}} \tag{55}$$

where $\hat{k}$ is the opposite direction of k.

By considering the condition of diffusive and grey walls and using the value of one for the emissivity coefficient ε_e [1], the boundary conditions of the radiative distribution function can be presented in the following forms:

- At the inlet section of the channel:

$$I_i = \frac{\sigma}{\pi}\theta_{in}^4 \tag{56}$$

- Over the channel wall:

$$I_i = \frac{\sigma}{\pi}\theta_w^4 \tag{57}$$

- At the outlet section of the channel:

$$I_i = \frac{\sigma}{\pi}\theta_o^4 \tag{58}$$

3.3. Extinction coefficient of porous medium

In this research, Silicon Carbide (SiC) is selected as the porous material. The extinction coefficient for the solid phase in the porous medium, presented by Guo and Zaho [42], can be evaluated by

$$\beta_s = 12.64(1-\varepsilon)^{0.7}/d_p^{0.79}, \tag{59}$$

where ε and d_p are the porosity and the pore size, respectively. The effective extinction coefficient for the porous medium, containing solid and fluid phases, can be written in the following form

$$\beta_e = \varepsilon\beta_f + (1-\varepsilon)\beta_s, \tag{60}$$

where β_f and β_s is the extinction coefficients of the fluid and solid phases, respectively.

3.4. Calculation of Nusselt number

To calculate the Nusselt number, the average temperature is used, which is defined by:

$$\theta_m = \int_A \rho u\theta dA / \int_A \rho u dA, \tag{61}$$

where θ_m is the mean temperature and u and θ are the local velocity and temperature, respectively. The Nusselt number on the wall of the channel can be calculated by:

$$Nu = (\frac{H}{\theta_w - \theta_m})(-\frac{\partial\theta}{\partial y}), \tag{62}$$

In this equation, θ_w and H are the wall temperature and the channel width, respectively.

3.5. Grid‑independency study

The sample grid used in the channel is shown in Fig. 5. As shown in this figure, the structured and square grids are used in this problem.

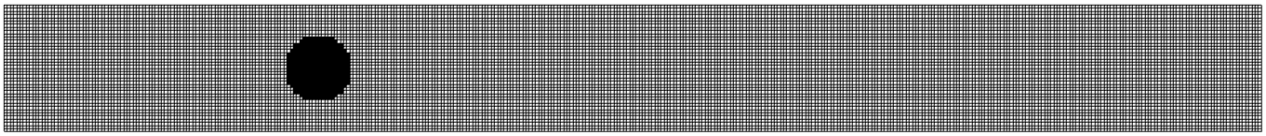

Fig. 5. The sample grid used in the channel.

In this paper, the GCI convergence criterion is also used to ensure about the grid‐independency of this problem [43-44]. In order to examine this criterion, it is assumed that the channel width is 10 mm. The velocity in x direction and the temperature at the centre of the porous medium for three grid numbers, including 20×200, 40×400, and 80×800, are calculated. The results of application of this criterion to this problem are presented in Table 1 for Re=10, Pr=0.744, ε=0.85, Da=0.1, N=0.03, and the radiation absorption coefficient of 0.1. According to Table 1, the GCI convergence criterion for the grid size of 40×400 has a negligible error and hence, this grid is used in the rest of this paper.

Table 1. The results of GCI convergence criterion for Re=10, Pr=0.744, ε=0.85, Da=0.1, N=0.03, and the radiation absorption coefficient of 0.1.

	U(2.5,0.5)	θ(2.5,0.5)
M1,M2,M3	64000,16000,4000	64000,16000,4000
r21	2	2
r32	2	2
Data1	1.417	0.906
Data2	1.419	0.906
Data3	1.423	0.893
P	1	2.459
φ_{ext}^{21}	1.415	0.90644
e_a^{21}(%)	0.1411	0.2207
e_{ext}^{21}(%)	0.1413	0.04854
GCI_{fine}^{21}(%)	0.1763	0.061341

Note that in this table M is the number of nodes in the computational domain, U and θ are the dimensionless velocity and the dimensionless temperature, respectively. Data indicates the

local values of each parameter and r is the ratio of the space step of each mesh size to the space step of previous mesh. The apparent order P of the technique can be calculated by:

$$\boldsymbol{P} = \frac{1}{ln(r21)}\left(ln\left(\frac{\epsilon 32}{\epsilon 21}\right) + \ln\left(\frac{r_{21}^{\mathbf{P}} - s}{r_{32}^{\mathbf{P}} - s}\right)\right), \tag{63}$$

$$s = 1\,.\,sgn(\epsilon 32/\epsilon 21), \tag{64}$$

where $\epsilon 21 = Data2 - Data1$ and $\epsilon 32 = Data3 - Data2$

The extrapolated values can be calculated by the following relation

$$\emptyset_{ext}^{21} = \frac{r_{21}^{\boldsymbol{P}} Data1 - Data2}{r_{21}^{\boldsymbol{P}} - 1}. \tag{65}$$

The approximate relative error is defined by:

$$e_a^{21} = \left|\frac{Data1 - Data2}{Data1}\right|, \tag{66}$$

and the extrapolated relative error is calculated through the following expression

$$e_{ext}^{21} = \left|\frac{\emptyset_{ext}^{21} - Data1}{\emptyset_{ext}^{21}}\right|. \tag{67}$$

Finally, the fine-grid convergence index is given by:

$$GCI_{fine}^{21} = \frac{1.25 e_a^{21}}{r_{21}^{\boldsymbol{P}} - 1}. \tag{68}$$

3.6. Validation

To evaluate the accuracy of the numerical results, the current results obtained by LBM is compared against the analytical data. Figure 6 shows the comparison of the results of the distributions of the dimensionless temperature obtained by the current LBM and an analytical solution presented by Talukdar et al. [45] for the combined radiation and convection heat transfer in a porous duct. It is noted that in this figure, the dimensionless temperature distribution has been plotted along the vertical line at the horizontal distance of X=0.05 from the channel inlet. As shown in this figure, there is a good agreement between the results obtained by the current LBM and the analytical solution.

The differences between the results of the present work and the analytical results are due to the simplifying assumptions made in the analytical paper [45]. These assumptions are:

1. In the analytical paper, the flow is fully developed from the inlet of the channel, while in the present work, a developing flow is considered.
2. The convection heat transfer along the channel height is ignored in the analytical paper.
3. In the analytical paper, the conduction heat transfer along the length of the channel is ignored.
4. Finally, the radiation heat transfer along the channel axis is also neglected in the analytical paper, while it has a significant contribution with heat transfer.

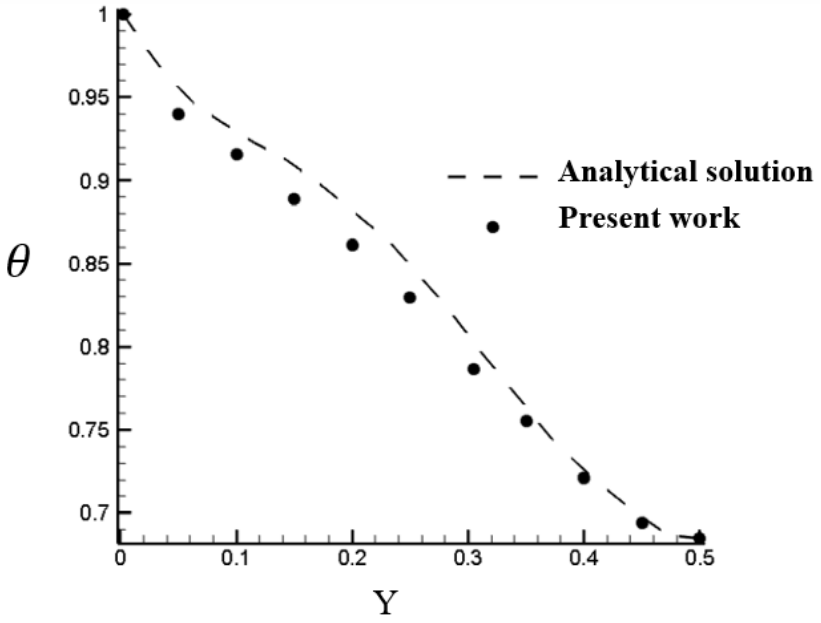

Fig. 6. A comparison between the results obtained by the current LBM and the analytical solution of Talukdar et al. [45] for the dimensionless temperature distribution along the vertical line at the X=0.05, ω=0.35, N=0.01, ε_g=1, Pe=8, and β=2.

For further validation, the fully developed velocity distribution inside a two-dimensional rectangular channel fully filled with a porous material is calculated by current LBM and compared with the numerical results of Mahmud and Fraser [46]. The results of this comparison

are plotted in Fig. 7 at different values of Darcy number and Re=100. An excellent agreement between the two set of numerical results is evident in this figure.

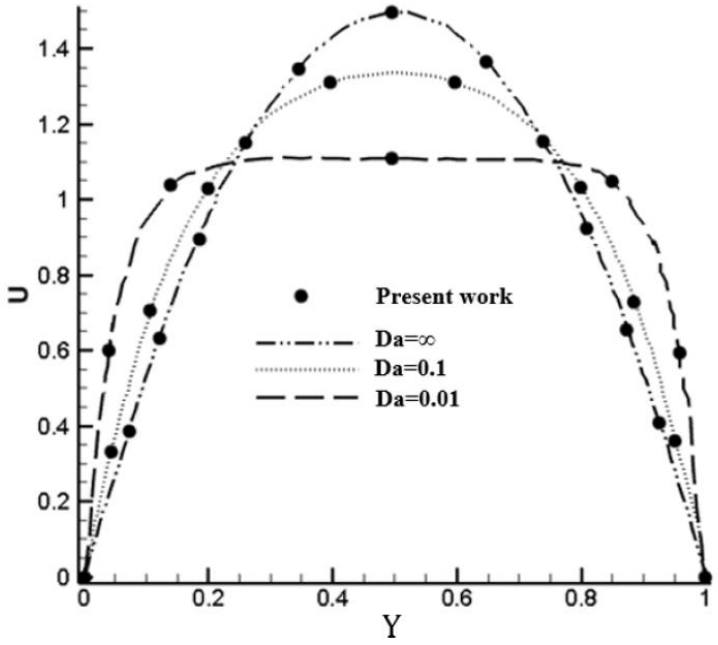

Fig. 7. A comparison between the results obtained by the current LBM and the numerical results of Mahmud and Fraser [46] for the fully developed velocity distribution inside a two-dimensional, rectangular channel fully filled with a porous material at different values of Darcy number and Re=100.

4. Result and discussion

The results of numerical simulations are presented in this section. The effects of different parameters including porosity and pore size of the porous medium and conduction radiation ratio on the flow and temperature fields are investigated.

Figure 8 shows the streamlines for different values of porosity. It is recalled that ε=1 indicates that there is no cylinder inside the channel. The streamlines are parallel and there is no deviation for the case of ε=1. For this trivial case, the flow is fully attached to the cylinder wall and there is no flow separation and recirculating wake developed downstream of the cylinder. The amount of fluid penetrated inside the porous cylinder is related to the porosity. A more permeable cylinder allows the fluid to flow inside it to experience a low resistance. This minimises the

deviation of streamlines around the cylinder wall. Figure 8 shows that the streamlines deviation increases as the porosity of the porous cylinder decreases. For the lower values of porosity (e.g. 0.85), two recirculation wakes are created at the downstream of the cylinder as the pressure is increased in the rear region of the cylinder and the flow receives the adverse pressure gradient and separates from the cylinder wall. By further decrease in porosity, the recirculation wakes are elongated.

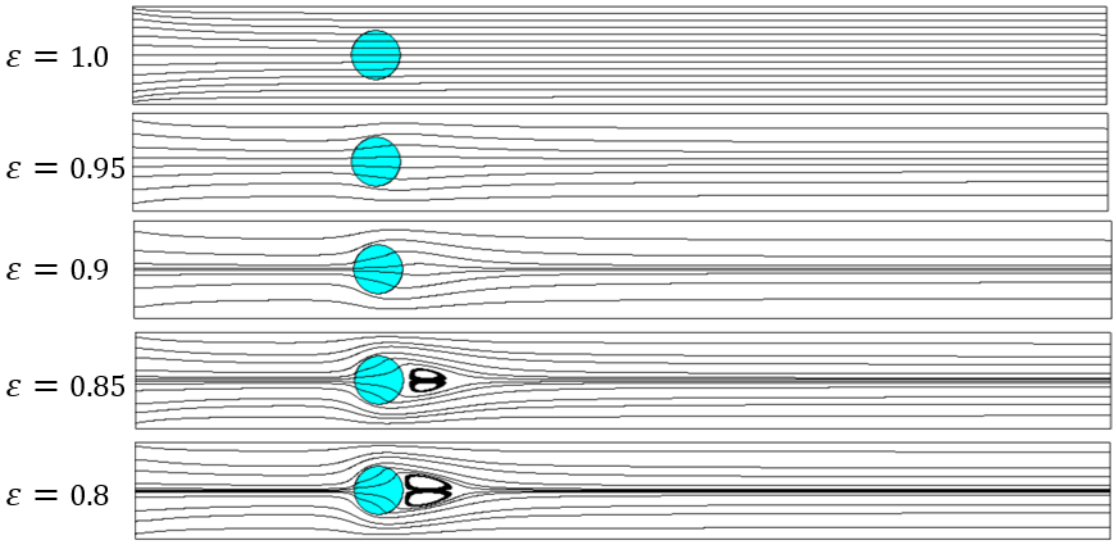

Fig. 8. Streamlines for different values of porosity $Re = 100,\ d_p = 0.9mm,\ j = 1$.

Figure 9 shows the dimensionless temperature contour for different values of porosity at $Re = 100,\ Pe = 74.4,\ d_p = 0.9mm,\ N = 0.03\ , j = 1\ ,\ \gamma = 1,\ \omega = 0,\ \varepsilon_e = 1$. As shown in this figure, the thermal plume is formed behind the porous cylinder. The thermal plume elongates as the porosity increases. As mentioned earlier, a more permeable cylinder allows more fluid to flow inside it and thus, the fluid carries away more heat from the cylinder surfaces. Moreover, this figure shows that as porosity decreases, the thermal development length around the walls of the channel reduces.

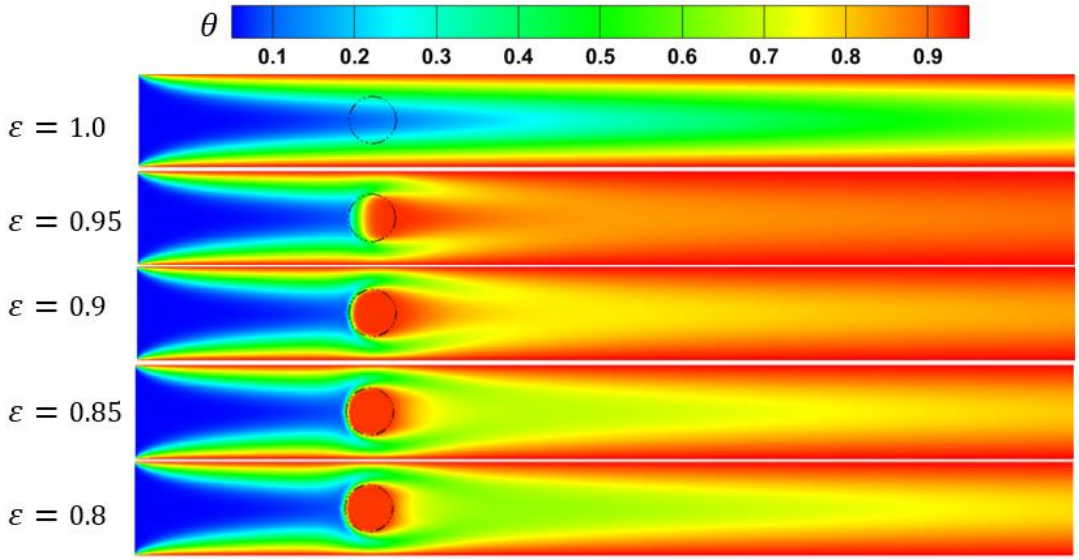

Fig. 9. The dimensionless temperature contour for different values of porosity at $Re = 100$, $Pe = 74.4$, $d_p = 0.9mm$, $N = 0.03$, $j = 1$, $\gamma = 1$, $\omega = 0$, $\varepsilon_e = 1$.

Figure 10 shows the local Nusselt number on the channel wall for different values of porosity at $Re = 100$, $Pe = 74.4$, $d_p = 0.9mm$, $N = 0.03$, $j = 1$, $\gamma = 1$, $\omega = 0$, $\varepsilon_e = 1$. As shown in this figure, the Nusselt number decreases on the channel wall by decreasing the porosity, which indicates the reduction of heat transfer along the channel length. The local Nusselt number, on the part of the channel wall that the porous cylinder is placed, enhances dramatically for all values of porosity. This indicates that the presence of porous cylinder enhances the heat transfer on the channel wall.

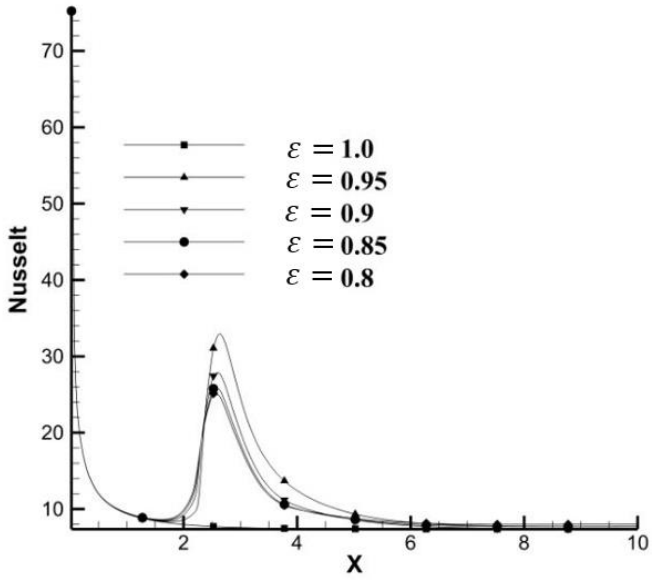

Fig. 10. The local Nusselt number on the channel wall for different values of porosity at $Re = 100,\ Pe = 74.4,\ d_p = 0.9mm,\ N = 0.03,\ j = 1,\ \gamma = 1,\ \omega = 0,\ \varepsilon_e = 1.$

Figure 11 shows the streamlines for different values of pore size. The permeability of the porous medium decreases with reducing the pore size. Accordingly, the streamlines deviations around the cylinder wall increase with decreasing the pore sizes. Further, for a very low pore size, two recirculation wakes are formed downstream of the cylinder due to the flow separation.

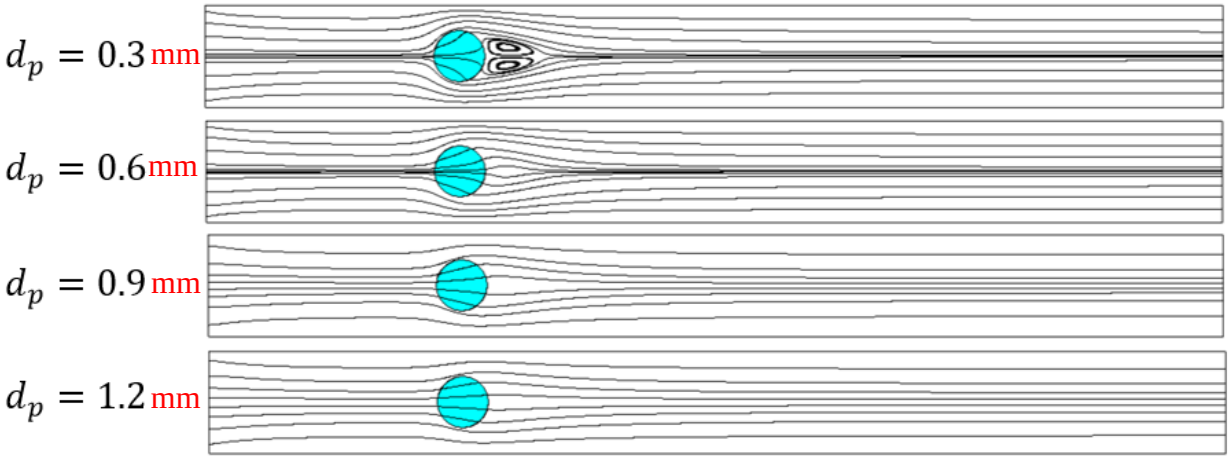

Fig. 11. Streamlines for different values of pore size at $Re = 100,\ j = 1,\ \varepsilon = 0.85.$

Figure 12 shows the dimensionless temperature distribution for different values of pore sizes. As shown in this figure, the thermal plume formed behind the porous cylinder elongates as the pore size increases. This means that the thermal penetration of porous cylinder increases with increasing the pore size. It is emphasised that the transport of heat is enhanced with increasing the pore size because the fluid flows faster through the internal pores of the porous cylinder.

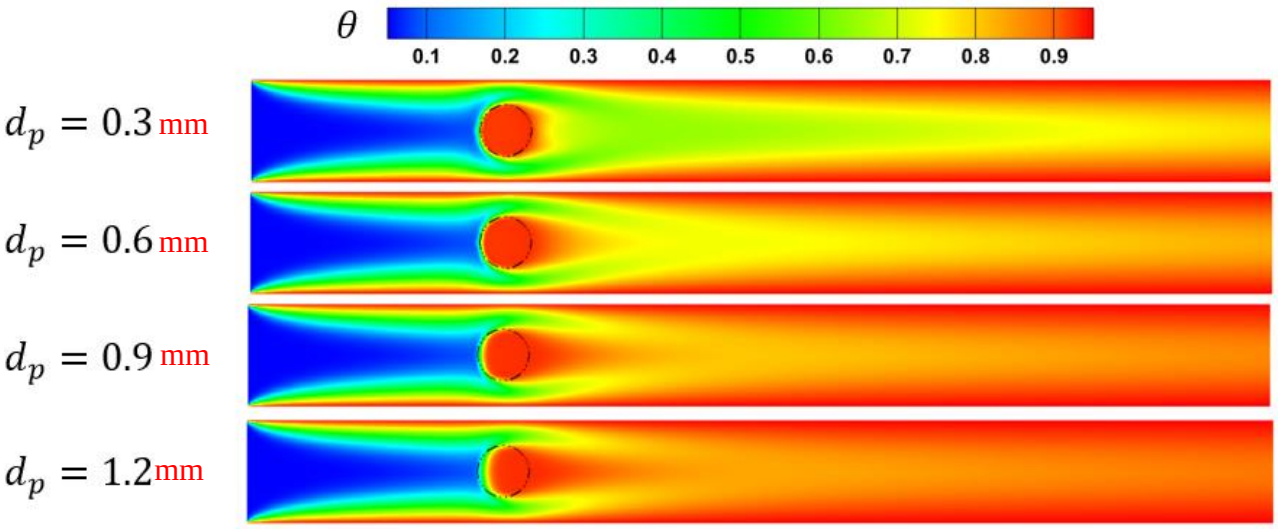

Fig. 12. The dimensionless temperature contour for different values of pore size at $Re = 100$, $Pe = 74.4$, $N = 0.03$, $j = 1$, $\gamma = 1$, $\varepsilon = 0.85$, $\omega = 0$, $\varepsilon_e = 1$.

Figure 13 shows the local Nusselt number on the channel wall for different values of pore size at $Re = 100$, $Pe = 74.4$, $d_p = 0.9mm$, $N = 0.03$, $j = 1$, $\gamma = 1$, $\omega = 0$, $\varepsilon_e = 1$. It can be seen that the Nusselt number decreases on the channel wall by increasing the pore size. Further, as the pore size increases, the values of Nusselt number converge, indicating a nonlinear relationship between the Nusselt number and the pore size.

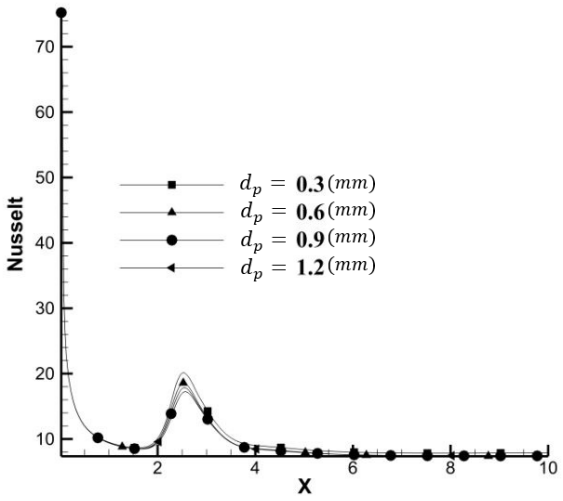

Fig. 13. The local Nusselt number on the channel wall for different values of pore size at $Re = 100$, $Pe = 74.4$, $N = 0.03$, $j = 1$, $\gamma = 1$, $\varepsilon = 0.85$, $\omega = 0$, $\varepsilon_e = 1$.

Figure 14 shows the dimensionless temperature distribution for different values of conduction-radiation ratio at $Re = 100$, $Pe = 74.4$, $d_p = 0.9mm$, $j = 1$, $\gamma = 1$, $\varepsilon = 0.85$, $\omega =$

0, and $\varepsilon_e = 1$. It can be seen that the temperature increases in the porous cylinder and downstream regions of the cylinder as the conduction-radiation ratio decreases. This provides smoother temperature gradients in the flow field. It is also noted that the radiation contribution increases as the conduction-radiation ratio decreases. The medium will absorb more radiation energy as the radiation contribution increases.

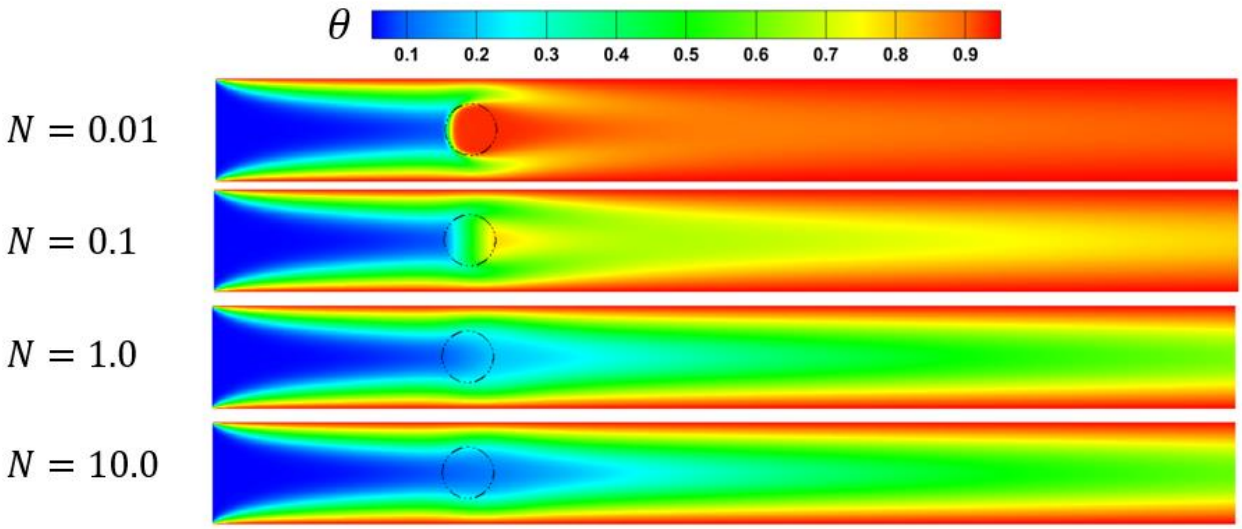

Fig. 14. The dimensionless temperature distribution for different values of conduction-radiation ratio at $Re = 100,\ Pe = 74.4,\ d_p = 0.9mm,\ j = 1,\ \gamma = 1,\ \varepsilon = 0.85,\ \omega = 0,$ and $\varepsilon_e = 1$.

Figure 15 shows the mean temperature distribution along the channel length for different values of conduction - radiation ratio. In this figure, X=2.5 indicates the location of the centre of the cylinder. The mean temperature decreases with increasing the values of conduction - radiation ratio for X>2.5. As already discussed, the radiation contribution decreases as the conduction radiation ratio increases. This leads to the absorption of a lower radiation energy and therefore, a reduction in the temperature.

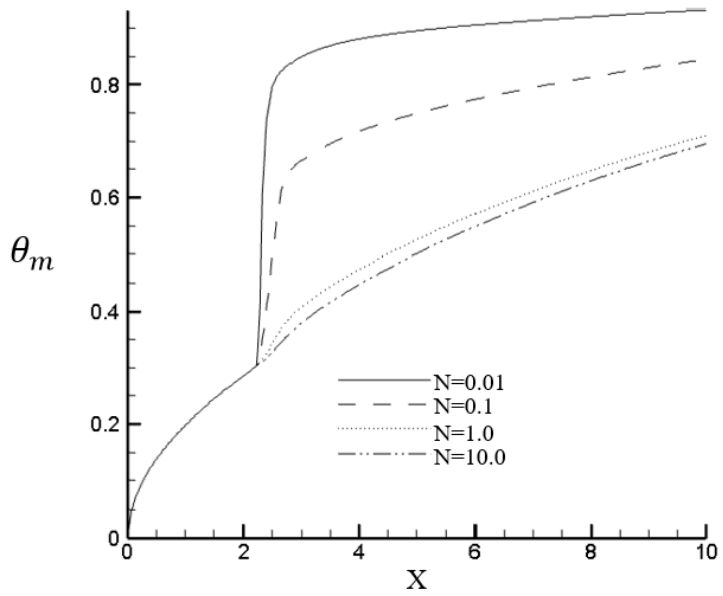

Fig. 15. Mean temperature distribution along the channel length for different values of conduction - radiation ratio at $Re = 100,\ Pe = 74.4,\ d_p = 0.9mm,\ j = 1,\ \gamma = 1,\ \varepsilon = 0.85,\ \omega = 0,\ \varepsilon_e = 1.$

Figure 16 discloses the local Nusselt number on the channel wall for different values of conduction-radiation ratio at $Re = 100,\ Pe = 74.4,\ d_p = 0.9mm,\ j = 1,\ \gamma = 1,\ \varepsilon = 0.85,\ \omega = 0,\ \varepsilon_e = 1.$ As shown in this figure, the Nusselt number decreases on the channel wall by increasing the conduction-radiation ratio. It is noted that the variations of the Nusselt number with the conduction-radiation ratio are very small. The maximum variations of the Nusselt number with the conduction-radiation ratio occurs on the part of the channel wall that the porous cylinder is placed on. In other parts of the channel length, the conduction-radiation ratio has a negligible effect on the Nusselt number.

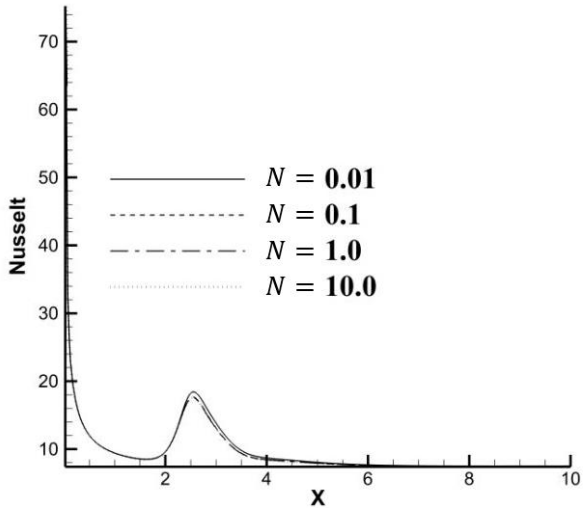

Fig. 16. The local Nusselt number on the channel wall for different values of conduction - radiation ratio at $Re = 100$, $Pe = 74.4$, $d_p = 0.9mm$, $j = 1$, $\gamma = 1$, $\varepsilon = 0.85$, $\omega = 0$, $\varepsilon_e = 1$.

Figure 17 depicts the streamlines for different values of kinematic viscosity ratio. The kinematic viscosity ratio represents the ratio of the effective kinematic viscosity of the porous medium to the kinematic viscosity of the fluid. This parameter directly affects the flow inside and outside of the porous cylinder and ultimately affects the heat transfer. As shown in Fig. 17, the penetration of flow inside the porous cylinder decreases as the kinematic viscosity ratio increases. This leads to the passage of the flow around the cylinder instead of penetrating inside it. As a result, the flow separation from the cylinder surface takes place and recirculation regions are formed for larger values of the effective kinematic viscosity. Finally, the lengths of wakes increase with increasing the kinematic viscosity ratio.

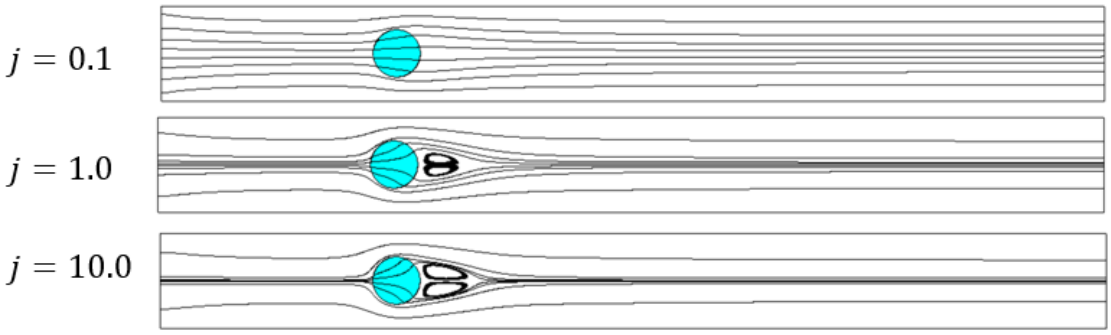

Fig. 17. Streamlines for different values of kinematic viscosity ratio at $Re = 100$, $Pe = 74.4$, $\gamma = 1$, $\omega = 0$, $\varepsilon = 0.85$, and $N = 0.03$.

The effects of kinematic viscosity ratio on the dimensionless temperature distribution are disclosed in Fig. 18. This figure shows that the thermal plume formed behind the porous cylinder shrinks and the thermal penetration of porous cylinder reduces with increasing the kinematic viscosity ratio. This could be due to the reduction of fluid penetration into the porous medium for larger values of kinematic viscosity ratio.

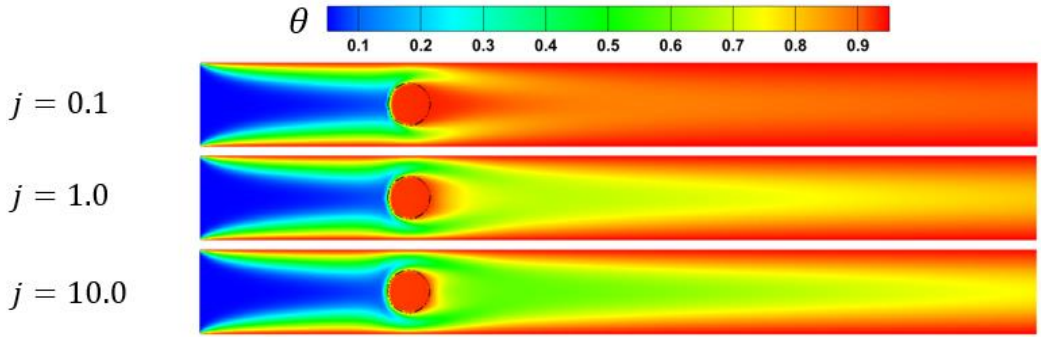

Fig. 18. The dimensionless temperature distribution for different values of kinematic viscosity ratio at $\mathrm{Re} = 100$, $Pe = 74.4$, $\gamma = 1$, $\omega = 0$, $\varepsilon = 0.85$, and $N = 0.03$.

The effects of kinematic viscosity ratio on the mean temperature distribution along the channel length are shown in Fig. 19. These effects are due to the reduction of fluid penetration into the porous medium. It is noted that the temperature of porous medium is higher than the inlet fluid temperature. Moreover, the reduction of fluid penetration into the porous medium reduces the heat transfer and the fluid contact with the inner surfaces of the porous medium. Consequently, the fluid flow only contacts with the outer surface of the porous cylinder and thus absorbs less heat from the porous cylinder. The mean temperature at the channel output decreases by about 19% as the kinematic viscosity ratio increases in the range of 0.1 to 10.

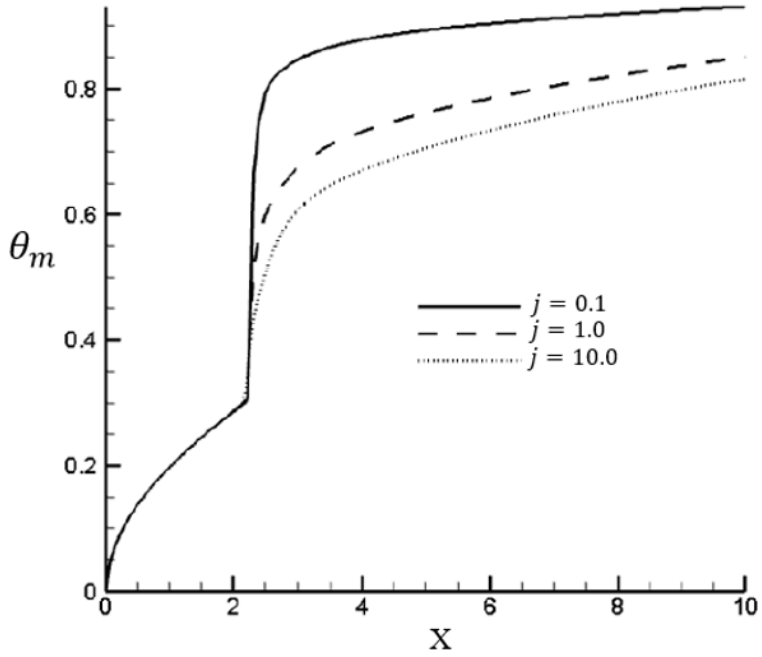

Fig. 19. Mean temperature distribution along the channel length for different values of kinematic viscosity ratio at $\mathrm{Re} = 100$, $Pe = 74.4$, $\gamma = 1$, $\omega = 0$, $\varepsilon = 0.85$, and $N = 0.03$.

The effects of kinematic viscosity ratio on the local Nusselt number on the channel wall at $\mathrm{Re} = 100$, $Pe = 74.4$, $\gamma = 1$, $\omega = 0$, $\varepsilon = 0.85$, and $N = 0.03$ are shown in Fig. 20. As shown in this figure, the Nusselt number decreases on the channel wall by increasing the kinematic viscosity ratio. Further, as the kinematic viscosity ratio decreases, the values of Nusselt number converge, indicating a nonlinear relationship between the Nusselt number and the kinematic viscosity ratio. The maximum variations of the Nusselt number with the kinematic viscosity ratio occurs on the part of the channel wall that the porous cylinder is placed on. In other parts of the channel length, the kinematic viscosity ratio has a negligible effect on the Nusselt number.

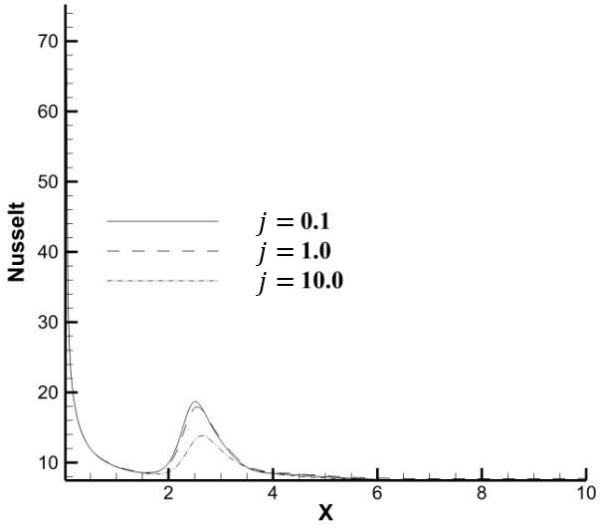

Fig. 20. The local Nusselt number on the channel wall for different values of kinematic viscosity ratio at $\mathrm{Re} = 100,\ Pe = 74.4, \gamma = 1,\ \omega = 0, \varepsilon = 0.85$, and $N = 0.03$.

Figure 21 discloses the dimensionless temperature distribution for different values of extinction coefficient of fluid. This figure shows that the thermal entrance length of the channel decreases as the extinction coefficient of fluid increases. Accordingly, the extinction coefficient of fluid strongly affects the channel temperature. As a result, for the processes in which the fluid is unable to absorb thermal radiation, the porous medium can recover this defect. However, the role of the porous medium in this regard decreases for the cases in which the fluid is capable of absorbing radiation.

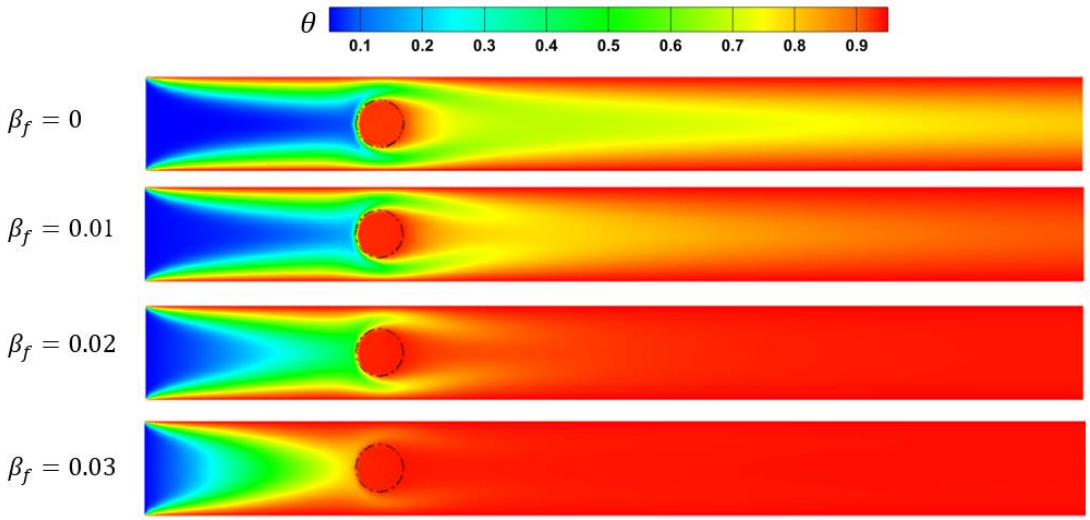

Fig. 21. The dimensionless temperature distribution for different values of extinction coefficient of fluid at $Re = 100, Pe = 74.4,\ j = 1,\ \omega = 0, \varepsilon = 0.85,$ and $\gamma = 1$.

Figure 22 shows the mean temperature distribution along the channel length for different values of extinction coefficient of fluid. It is inferred from this figure that the thermal entrance length of the channel decreases with increasing the extinction coefficient of fluid. It is recalled that the effective extinction coefficient of the porous medium is a function of the extinction coefficient of fluid. Hence, change of the the extinction coefficient of fluid directly affects the absorption of porous media, which is clearly seen in this figure. The mean temperature at the channel output increases by about 22% as the extinction coefficient of fluid increases in the range of 0 to 0.03.

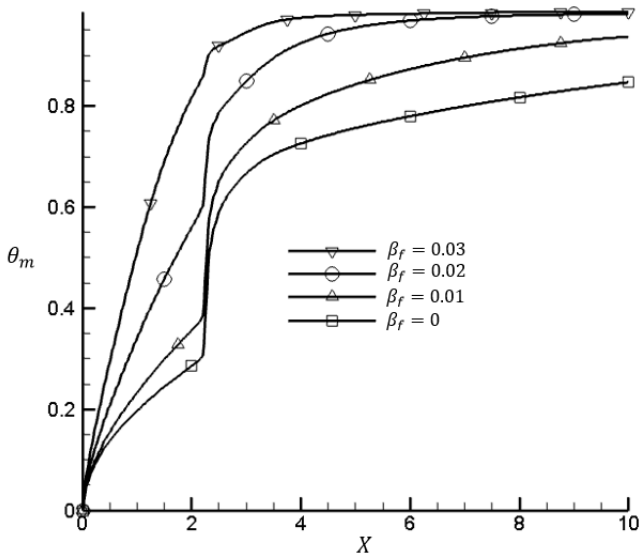

Fig. 22. Mean temperature distribution along the channel length for different values of extinction coefficient of fluid at $Re = 100$, $Pe = 74.4$, $j = 1$, $\omega = 0$, $\varepsilon = 0.85$, and $\gamma = 1$.

The effects of extinction coefficient of the fluid upon the local Nusselt number on the channel wall at $Re = 100$, $Pe = 74.4$, $j = 1$, $\omega = 0$, $\varepsilon = 0.85$, and $\gamma = 1$ are shown in Fig. 23. As shown in this figure, the Nusselt number on the part of the channel wall upstream of the porous cylinder decreases by increasing the extinction coefficient of fluid. However, a reverse procedure happens on the part of the channel located downstream of the porous cylinder. For the part of the channel wall that the porous cylinder is placed, the extinction coefficient of fluid has a negligible effect on the Nusselt number. Moreover, as the extinction coefficient of fluid

decreases, the values of Nusselt number converge, indicating a nonlinear relationship between the Nusselt number and the extinction coefficient of fluid.

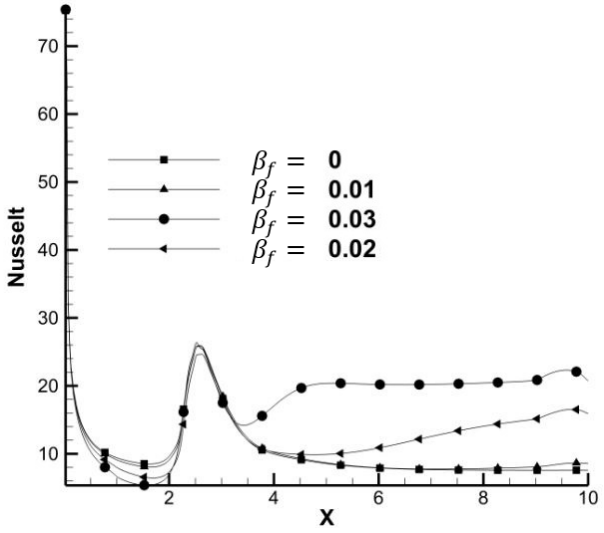

Fig. 23. The local Nusselt number on the channel wall for different values of extinction coefficient of fluid at $Re = 100$, $Pe = 74.4$, $j = 1$, $\omega = 0$, $\varepsilon = 0.85$, and $\gamma = 1$.

Finally, it was observed that the Nusselt number and the average temperature reduce by increasing the conduction-radiation ratio. The same procedure was reported by McCulloch [47]. Further, it was concluded that the average temperature increases with increasing the extinction coefficient of fluid, in agreement with that reported by Talukdar et al. [48]. Similar to the work of Talukdar et al. [48], it was observed that the Nusselt number decreases on the channel wall by increasing the pore size.

5. Conclusions

In this paper, a lattice Boltzmann method was used to simulate the conjugate radiation-forced convection heat transfer in a porous medium. The main findings of this work are summarized in the followings.

- There is a good agreement between the results obtained by the current LBM and the analytical solution for this problem.

- The streamlines deviation increases as the porosity of the porous cylinder decrease. For lower values of porosity (e.g. 0.85), two recirculation wakes are formed downstream of the cylinder.
- Increasing the pore size results in decreasing the Nusselt number on the channel wall.
- The Nusselt number decreases on the channel wall by decreasing the porosity and by increasing the kinematic viscosity ratio.
- The temperature increases in the porous cylinder and downstream regions of the cylinder as the conduction-radiation ratio decreases.
- The mean temperature at the channel output decreases by about 19% as the kinematic viscosity ratio increases in the range of 0.1 to 10.
- The mean temperature at the channel output increases by about 22% as the extinction coefficient of the fluid increases in the range of 0 to 0.03.

Appendix A

The descriptions about the procedure of mass flow rate control in LBM are provided in this Appendix. The mass flow rate at the entrance of the channel is calculated as follows:

$$\dot{m}_{in} = \int_0^H \rho u_{in} dA \tag{A1}$$

where, ρ, $\dot{m}_{in}$, u_{in}, and dA are the fluid density, the mass flow rate at the entrance of the channel, fluid velocity at entrance of the channel, and the surface element normal to the channel axis, respectively.

Further, the mass flow rate at each cross section of the channel is defined as follows:

$$\dot{m}_{section} = \int_0^H \rho u_{section} dA \tag{A2}$$

$$\frac{u_{section}^{new}}{u_{in}} = \frac{u_{section}^{old}}{u_{in}} + URF \times \frac{\frac{(\dot{m}_{in} - \dot{m}_{section})}{\rho}}{u_{in} \times H \times Re^2} \tag{A3}$$

$$\frac{u_{section}^{new}}{u_{in}} = \frac{u_{section}^{old}}{u_{in}} + URF \times \Delta u^+ \tag{A4}$$

$$\Delta u^{+} = \frac{(\dot{m}_{in} - \dot{m}_{section})}{\rho \times u_{in} \times H \times Re^{2}} \quad \text{(A5)}$$

where $u_{section}, \dot{m}_{section}$, and URF are the local velocity distribution at each cross section of the channel, the mass flow rate at each cross section of the channel, and the under relaxation factor, respectively. Eventually, the difference between the flow rates at the entrance of the channel and an arbitrary cross section is positive if the flow rate at that cross section to be lower than the flow rate of the entrance. This causes an increment in the velocity of that cross section and also leads to a significant improvement in the convergence speed.

Appendix B

The following equation is used to calculate the velocity in the porous medium [49]:

$$\rho u = \sum_{k} c_k f_k + \frac{\Delta t}{2} \rho F \quad \text{(B1)}$$

where $F = -\frac{\varepsilon \upsilon_e}{K} u - \frac{\varepsilon F_\varepsilon}{\sqrt{K}} |u| u$ is the external force exerted by the porous medium. By placing the value of this force in Eq. B1, the following equation can be derived:

$$\rho u = \sum_{k} c_k f_k + \frac{\Delta t}{2} \rho \left(-\frac{\varepsilon \upsilon_e}{K} u - \frac{\varepsilon F_\varepsilon}{\sqrt{K}} |u| u\right) \quad \text{(B2)}$$

The Eq. B2 is a nonlinear relation. By rewriting this equation, the following equation can be obtained:

$$\rho \frac{\Delta t}{2} \frac{\varepsilon F_\varepsilon}{\sqrt{K}} |u| u + \rho \left(1 + \frac{\Delta t}{2} \frac{\varepsilon \upsilon_e}{K}\right) u - \rho \left(\frac{\sum_k c_k f_k}{\rho}\right) = 0 \quad \text{(B3)}$$

By considering $c_1 = \frac{\Delta t}{2} \frac{\varepsilon F_\varepsilon}{\sqrt{K}}$, $c_0 = \frac{1}{2}\left(1 + \varepsilon \frac{\Delta t}{2} \frac{\upsilon_f}{K}\right)$, and $\boldsymbol{v} = \frac{\sum_k c_k f_k}{\rho}$, Eq. B3 can be rewritten in the following form:

$$\rho c_1 |u| u + 2\rho c_0 u - \rho \boldsymbol{v} = 0 \quad \text{(B4)}$$

By assuming non-zero density, Eq. B4 can be simplified as follows:

$$c_1 |u| u + 2c_0 u - \boldsymbol{v} = 0 \rightarrow u = \frac{\boldsymbol{v}}{c_1 |u| + 2c_0} \quad \text{(B5)}$$

The denominator of this equation is a scalar. The following quadratic equation with respect to |u| can be achieved:

$$|u| = \frac{|v|}{c_1|u|+2c_0} \rightarrow c_1|u|^2 + 2c_0|u| - |\boldsymbol{v}| = 0 \quad \text{(B6)}$$

The roots of this equation are:

$$|u| = -\frac{1}{c_1}(c_0 \pm \sqrt{c_0^2 + c_1|\boldsymbol{v}|}) \quad \text{(B7)}$$

$|u|$ is a positive value and accordingly, the second root is acceptable. By placing it into Eq. B5, the velocity in the porous medium can be obtained as follows:

$$u = \frac{\boldsymbol{v}}{c_0+\sqrt{c_0^2+c_1|\boldsymbol{v}|}} \quad \text{(B8)}$$

Compliance with ethical standards

Conflict of Interest

All authors declare that they have neither conflict of interest, nor external funding.

References

References

[1] Hosseini, R., Rashidi, S., and Esfahani, J. A. A lattice Boltzmann method to simulate combined radiation–force convection heat transfer mode. Journal of the Brazilian Society of Mechanical Sciences and Engineering, 1-12, 2017.

[2] Nazari, M., and Ramzani, S. Cooling of an electronic board situated in various configurations inside an enclosure: lattice Boltzmann method. Meccanica, 49(3), 645–658, 2014.

[3] Amiri Rad, E., and Salimi, M. Investigating the effects of shear rate on the collapse time in a gas–liquid system by lattice Boltzmann. Meccanica, 52(4-5), 915–924, 2017.

[4] Muley, A., Kiser, C., Sundén, B., and Shah, R.K. Foam heat exchangers: a technology assessment. Heat Transfer Engineering. 33, 42-51, 2012.

[5] Rashidi, S., Esfahani, J.A., and Karimi, N. Porous materials in building energy technologies—A review of the applications, modelling and experiments. Renewable and Sustainable Energy Reviews. 91, 229-247, 2018.

[6] Rashidi, S., Esfahani J.A., and Rashidi, A. A review on the applications of porous materials in solar energy systems. Renewable and Sustainable Energy Reviews. 73, 1198-1210, 2017.

[7] Qin, J., Zhou, X., Zhao, C.Y., and Xu, Z.G. Numerical investigation on boiling mechanism in porous metals by LBM at pore scale level. International Journal of Thermal Sciences, 130, 298–312, 2018.

[8] Lei, H., Dong, L., Ruan, C., and Ren, L. Study of migration and deposition of micro particles in porous media by Lattice-Boltzmann Method. Energy Procedia, 142, 4004–4009, 2017.

[9] Dai, Q., and Yang, L. LBM numerical study on oscillating flow and heat transfer in porous media. Applied Thermal Engineering, 54, 16-25, 2013.

[10] Kefayati, G.H.R., Tang, H., Chan, A. and Wang, X. A. Lattice Boltzmann model for thermal non-Newtonian fluid flows through porous media. Computers and Fluids, 176, 226-244, 2018.

[11] Ma, Q., and Chen, Z. Numerical study on gas diffusion in isotropic and anisotropic fractal porous media (gas diffusion in fractal porous media). International Journal of Heat and Mass Transfer, 79, 925–929, 2014.

[12] Yun, H., M.A, F., Guo, X., and Chen, B. Mesoscopic pore-scale simulations of natural convection of porous media in closed square cavity by using LBM. Procedia Engineering, 205, 4009–4016, 2017.

[13] Jiang, P. X., Si, G. S., Li, M., & Ren, Z. P. Experimental and numerical investigation of forced convection heat transfer of air in non-sintered porous media. Experimental Thermal and Fluid Science, 28(6), 545-555, 2004.

[14] Thakur, N. S., Saini, J. S., and Solanki, S. C. Heat transfer and friction factor correlations for packed bed solar air heater for a low porosity system. Solar Energy, 74(4), 319-329, 2003.

[15] Dehghan, M., Rahmani, Y., Domiri Ganji, D., Saedodin, S., Valipour, M. S., and Rashidi, S. Convection-radiation heat transfer in solar heat exchangers filled with a porous medium: Homotopy perturbation method versus numerical analysis. Renewable Energy, 74, 448-455, 2015.

[16] Bovand, M., Rashidi, S., and Esfahani, J. A. Heat transfer enhancement and pressure drop penalty in porous solar heaters: Numerical simulations. Solar Energy, 123, 145-159, 2016.

[17] Parmananda, M., Dalal, A., and Natarajan, G. The influence of partitions on predicting heat transfer due to the combined effects of convection and thermal radiation in cubical enclosures. International Journal of Heat and Mass Transfer, 121, 1179-1200, 2018.

[18] Gao, D., Chen, Z., Chen, L., and Zhang, D. A modified lattice Boltzmann model for conjugate heat transfer in porous media. International Journal of Heat and Mass Transfer, 105, 673-683, 2017.

[19] Vijaybabu, T.R., Anirudh, K., and Dhinakaran, S. LBM simulation of unsteady flow and heat transfer from a diamond-shaped porous cylinder. International Journal of Heat and Mass Transfer, 120, 267-283, 2018.

[20] Chen S., and Doolen G. D. Lattice Boltzmann Method for Fluid Flows. Annual Review of Fluid Mechanics, 30(1), 329-364, 1998.

[21] He X., and Luo L.-S. Theory of the Lattice Boltzmann Method: From the Boltzmann Equation to the Lattice Boltzmann Equation. Physical Review E, 56(6) 6811-6817, 1997.

[22] Nithiarasu, P., Seetharamu, K.N., and Sundararajan, T. Natural convective heat transfer in a fluid saturated variable porosity medium. International Journal of Heat and Mass Transfer, 40, 3955 – 3967, 1997.

[23] Pepona, M., and Favier, J. A coupled Immersed Boundary-Lattice Boltzmann method for incompressible flows through moving porous media. Journal of Computational Physics, 321, 1170-1184, 2016.

[24] Li, Q., He, Y. L., Tang, G. H., and Tao, W. Q. Improved axisymmetric lattice Boltzmann scheme. Physical Review E, 81, 056707, 2010.

[25] Guo Z., and Zhao T.S. Lattice Boltzmann model for incompressible flows through porous media. Phys. Rev., E 66, 036304, 2002.

[26] Guo, Z., and Zheng, C., Shi, B. Discrete lattice effects on the forcing term in the Lattice Boltzmann method, Phys. Rev., E 65, 046308, 2002.

[27] Hsu, C.T., and Cheng, P. Thermal dispersion in a porous medium, International Journal of Heat and Mass Transfer, 33(8), 1587-1597, 1990.

[28] Ergun, S. Fluid flow through packed columns. Chemical Engineering Progress, 48, 89-94, 1952.

[29] Vafai, K. Convective flow and heat transfer in variable-porosity media. Journal of Fluid Mechanics, 147, 233-259, 1984.

[30] Yan, Y.Y., and Zu, Y.Q. Numerical simulation of heat transfer and fluid flow past a rotating isothermal cylinder — a LBM approach. International Journal of Heat and Mass Transfer, 51, 2519–2536, 2008.

[31] Mishra, S.C., Lankadasu, A., and Beronov, K. Application of the lattice Boltzmann method for solving the energy equation of a 2-D transient conduction radiation problem. International Journal of Heat and Mass Transfer, 48, 3648–3659, 2005.

[32] Raj, R., Prasad, A., Parida, P.R., and Mishra S.C. Analysis of solidification of a semi-transparent planar layer using the lattice Boltzmann method and the discrete transfer method. Numerical Heat Transfer, Part A: Applications, 49, 279–299, 2006.

[33] Mishra, S.C., and Roy, H.K. Solving transient conduction-radiation problems using the lattice Boltzmann method and the finite volume method. Journal of Computational Physics, 233, 89–107, 2007.

[34] Howell, J.R., Siegel, R., and Menguc, M.P. Thermal Radiation Heat Transfer, 5th ed., CRC Press, Florida, 2011.

[35] Modest, M.F. Radiative Heat Transfer, 3 ed. New York: Academic Press, 2003.

[36] Mishra, S.C. Asinari, P. and Borchiellini, R. A lattice Boltzmann formulation for the analysis of radiative heat transfer problems in a participating medium. Numerical Heat Transfer, Part B: Fundamentals, 57, 126-146, 2010.

[37] Asinari, P., Mishra, S. C., and Borchiellini, R. A lattice Boltzmann formulation for the analysis of radiative heat transfer problems in a participating medium. Numerical Heat Transfer, Part B: Fundamentals, 57(2), 126-146, 2010.

[38] Succi, S. The Lattice Boltzmann Method for Fluid Dynamics and Beyond, Oxford University Press, New York, 2001.

[39] Modest, M.F. Radiative Heat Transfer, third ed., Academic press, New York, 2013.

[40] Mishra, S.C., Roy, H.K., and Mishra, N. Discrete ordinate method with a new and a simple quadrature scheme. Journal of Quantitative Spectroscopy & Radiative Transfer, 101, 249–262, 2006.

[41] Sukop, M. C. DT Thorne, Jr. Lattice Boltzmann Modeling Lattice Boltzmann Modeling, 2006.

[42] Guo, Z., and Zhao, T. S. A lattice Boltzmann model for convection heat transfer in porous media. Numerical Heat Transfer, Part B, 47(2), 157-177, 2005.

[43] Roache, P. J. Verification and validation in computational science and engineering. Hermosa, 1998.

[44] Celik, I.B., Ghia, U., Roache, P.J., Freita, Ch. J.S., Coleman, H., and Raad, P. E., Procedure for estimation and reporting of uncertainty due to discretization in CFD applications. ASME Journal of Fluids Engineering, 130, 078001, 2008.

[45] Talukdar, P., Mishra, S. C., Trimis, D., & Durst, F. Combined radiation and convection heat transfer in a porous channel bounded by isothermal parallel plates. International Journal of Heat and Mass Transfer, 47(5), 1001-1013, 2004.

[46] Mahmud, S., and Fraser, R. A. Flow, thermal, and entropy generation characteristics inside a porous channel with viscous dissipation. International Journal of Thermal Sciences, 44(1), 21-32, 2005.

[47] McCulloch, R. Advances in radiation transport modeling using Lattice Boltzmann Methods (Doctoral dissertation, Kansas State University), 2015.

[48] Talukdar, P., Mishra, S. C., Trimis, D., and Durst, F. Combined radiation and convection heat transfer in a porous channel bounded by isothermal parallel plates. International Journal of Heat and Mass Transfer, 47, 1001-1013, 2004.

[49] Guo, Z., and Zhao, T.S. Lattice Boltzmann model for incompressible flows through porous media. Phys. Rev. E, 66, 036304, 2002.